

FERMAT'S PRINCIPLE, CAUSTICS, AND THE CLASSIFICATION OF GRAVITATIONAL LENS IMAGES

ROGER BLANDFORD AND RAMESH NARAYAN

Theoretical Astrophysics, California Institute of Technology, Pasadena

Received 1985 June 19; accepted 1986 April 24

ABSTRACT

Some general features of gravitational lensing of cosmologically distant objects by intervening masses are described. When the lensing mass distribution is restricted to a thin slab between the source and the observer, a time-delay surface can be constructed, allowing one to compute efficiently, via Fermat's principle, the image positions, magnifications, and parities for any background source location. Conditions under which the absolute image parities can be observationally determined are elucidated, and it is shown that only certain combinations of parities and delays are allowed when the lens is nonsingular and transparent. It is demonstrated that an image corresponding to a minimum (maximum) in the time-delay surface must have passed through less than (more than) a critical surface density of matter. Also, it is shown that a lens with a point singularity (e.g., a black hole) can sometimes be observationally distinguished from one with a line singularity (e.g., a cosmic string) using the parities of the observed images. Different possible arrangements of images are distinguished in terms of the topology of the "critical" contours that pass through saddle points in the time surface. It is argued that caustics, which involve the transition from one topology to another through the merger/creation of images, are important in the study of gravitational lensing. Fold and cusp caustics are analyzed, and it is shown that high-amplification images are most often associated with fold caustics. The extension of these ideas to multiple lenses and an inhomogeneous universe is outlined. The importance of seeking multiply imaged galaxies in the neighborhood of known multiply imaged quasars is emphasized.

Subject headings: galaxies: clustering — gravitation — quasars — relativity

1. INTRODUCTION

The recent discovery of at least six convincing examples of gravitational lens action has rekindled interest in the formal description of this effect (see Gunn 1981; Peacock 1983; Burke 1984; Turner, Ostriker, and Gott 1984, for recent theoretical and observational reviews). Much of this interest has been motivated by the difficulty of inferring the distribution of the lensing mass in the known examples. In no case has this been carried out noncontroversially. The large image separations that are seen suggest that extremely high velocity dispersion galaxies or groups of galaxies may be involved in the lensing. However, such objects are generally not seen even in deep searches of the field around the lensed images, suggesting that dark matter may be primarily responsible for lensing. Another intriguing feature is the occurrence of an even number of images in most of the known examples (with the exception of Q2016+112 [see Schneider *et al.* 1986] and possibly Q0957+561 [see Gorenstein *et al.* 1983]), in conflict with the well-known result (e.g., Burke 1981) that nonsingular lenses should produce an odd number. It is therefore a matter of immediate practical concern to explore different methods of performing the inversion from the observed image configuration to the mass distribution in the lensing plane. In this paper we describe the application of Fermat's principle of geometrical optics to the problem—an approach which we believe has some didactic and practical merit (cf. Schneider 1985). In particular, we show how it provides both a basis for a topological classification of possible image arrangements and a heuristic procedure for understanding the qualitative form of the underlying lensing mass distribution. We then go on to discuss the relevance of caustics to gravitational lensing. Further

insights into the application of Fermat's principle to this problem will be presented in Nityananda (1986).

Bourassa and Kantowski (1975) showed how to locate the position of the images on the sky when a point source (e.g., a quasar) was viewed from a cosmological distance through a single transparent galaxy (or cluster potential). They gave a vector (or equivalently a complex) equation for the displacement of the image on the sky, which had to be solved implicitly to obtain the actual ray(s). If we regard the objects as being of finite extent, then this equation defines a mapping from the object plane to the image plane. In general this mapping is one-to-many. The Jacobian of the transformation gives the ratio of elemental areas in the two planes, and, since surface brightness is preserved, it therefore also gives the effective magnification of the image. Further, the sign of the Jacobian gives the parity of the image. This vector approach forms the basis of almost all contemporary discussions.

In § II we describe an alternative, though equivalent, scalar description of gravitational lensing based on Fermat's principle, and reexpress the above features in this language. We assume that the lensing mass is confined to a single plane between the source and the observer and associate a time delay with each position in the sky of a potential image. The extrema of this time surface then give the true positions of the images. We state some general relationships between the magnifications, parities, and time delays of the images. In § III we explain a topological classification of image configurations and specialize our results to the cases of three- and five-image lensing geometries. One of our two independent three-image topologies corresponds to the standard lensing geometry due to a spherically symmetric lens, which has been discussed in the

literature (e.g., Young *et al.* 1980). However, the other three-image topology that we identify does not seem to have been distinguished so far. It can be produced by an elliptical (galaxy) lens or, in a limit, by a straight string. In § IV we describe a computer-graphical approach to the study of lensing by model galaxies and clusters. This can be used to model observed cases of lensing. We also outline the design of a simple optical apparatus which could be used for fast modeling of image geometries. In § V we develop the connection between the Fermat approach and the classical theory of caustics and the more recent general theory of catastrophes (Thom 1975; Berry and Upstill 1980). We identify the fold catastrophe as the most relevant for applications in gravitational lensing. Lensed images are greatly magnified in the vicinity of caustics. For a sufficiently steep quasar luminosity function, high-amplification events will determine lensing cross sections, as emphasized by Turner, Ostriker, and Gott (1984), and this is the motivation behind this and other recent studies of the structure of caustics (Nityananda and Ostriker 1984; Hogan and Narayan 1984). We point out that circularly symmetric geometries may be misleading, since they lead to a nongeneric caustic structure. In § VI we consider the extension of our results to multiple scattering, where the lensing mass is distributed in several planes, or continuously between the observer and the source. Many of our results survive in the case where there is one dominant lens, with the rest of the scattering acting as a perturbation. However, in the more general case when there are several dominant lenses, only some of our results remain true. We discuss future applications of these ideas in § VII.

II. FERMAT'S PRINCIPLE

If we consider all paths from a source S to the observer located at O (Fig. 1), then for each path we can form a path integral which measures the time of arrival of light at O leaving S at some fixed time. Fermat's principle states that this time is extremized when the path corresponds to an actual ray. In what follows, we assume the existence of angular diameter distances that relate a proper distance at the source to the angle it subtends at the observer, as is true for instance in a homogeneous cosmological model. Some modifications are needed when the matter is not smoothly distributed (e.g., Zel'dovich 1964; Dyer and Roeder 1973; see also § VI). We also require that the lensing potential be stationary for the time it takes light to cross it. This can be a limitation in the case of lensing by cosmic strings (e.g., Vilenkin 1984; Gott 1984; Hogan and Narayan 1984).

Let us specialize to the case where the lensing mass distribution is restricted to a thin slab between the source at redshift z_S and the observer. (We shall relax this condition in § VI.) We can idealize the situation further by taking a projected two-dimensional density distribution on a "lens plane" at redshift z_L . Consider now the set of paths which propagate along null geodesics of the uniform background universe from S to points on the lens plane, and then again along null geodesics from there to O . This family of paths is parameterized by the two-dimensional angular coordinate θ_I of the ray received at O ; we measure θ_I with respect to an arbitrary origin, which is most conveniently chosen to be the "center" of the lens. For a given path, there are two sources of time delay (cf. Schneider 1985). The geometrical contribution is just the extra path length traveled by the light when it is deflected from a geodesic in the background world model by a large mass. The second contribution, viz., the local gravitational time delay attributable to the presence of that mass, is familiar from the radar-ranging experiments carried out in the solar system (e.g., Reasenberg *et al.* 1979; Weinberg 1972).

Let d_{OS} and d_{OL} be the angular diameter distances of the source and the lens from the observer, and let the angular diameter distance of the source from the lens be d_{LS} . Let the angular position of the source in the sky be θ_S , defined to be the direction along which a ray would have been received in the absence of the lens. Consider the ray path shown in Figure 1 which is bent by an angle α at the lens plane and arrives at the observer along the direction θ_I . In the small-angle approximation, the geometrical time delay due to the extra path length of the ray as compared with the direct ray from S to O is measured by an observer in the lens plane to be $\alpha\xi/2$ (Fig. 1), where here and henceforth we set $G = c = 1$. Noting that $\xi = (\theta_I - \theta_S)d_{OL}$ and inserting a redshift factor, we find that the observed time delay is

$$t_{\text{geom}}(\theta_I; \theta_S) = \frac{(1 + z_L)d_{OL}d_{OS}}{2d_{LS}} (\theta_I - \theta_S)^2. \quad (2.1)$$

The gravitational time delay is given in the lens frame by $-2 \int ds \varphi(\theta_I)$, where φ is the local Newtonian potential and the integral is along the ray (e.g., Weinberg 1972; Misner, Thorne, and Wheeler 1973). (Arbitrary constants in the local definition of the potential are irrelevant.) The time delay in the observer frame is thus

$$t_{\text{grav}}(\theta_I) = -2(1 + z_L) \int ds \varphi(\theta_I). \quad (2.2)$$

The integral of the Newtonian potential along the line of sight

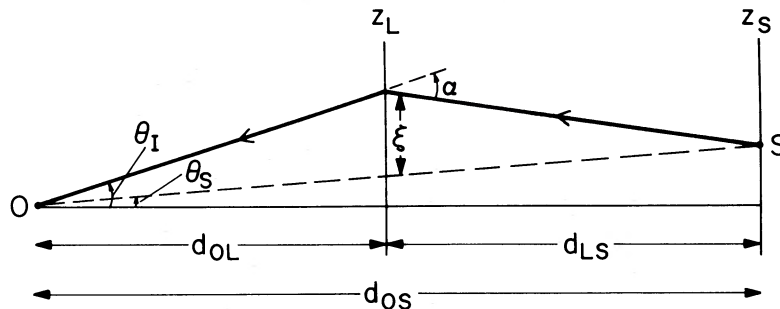


FIG. 1.—A ray from the source S at redshift z_S being gravitationally deflected through an angle α by the lens at redshift z_L before being received by the observer O . The image is located at an angular position θ_I , measured relative to an arbitrarily chosen reference direction. In the absence of the lens, the source would be seen at position θ_S . The angular diameter distances d_{OL} , d_{OS} , and d_{LS} are marked.

is a two-dimensional potential with the projected surface density as its source. Let us write

$$\tau = \frac{d_{LS}}{(1+z_L)d_{OL}d_{OS}} t \quad (2.3)$$

and define a two-dimensional relativistic potential $\psi(\theta_I)$ by

$$\psi(\theta_I) = \frac{2d_{LS}}{d_{OL}d_{OS}} \int ds \varphi(\theta_I) = \frac{4d_{LS}d_{OL}}{d_{OS}} \int d^2\theta' \Sigma(\theta') \ln(\theta_I - \theta'), \quad (2.4)$$

where $\Sigma(\theta')$ is the surface density (g cm^{-2}) of matter at relative position θ' . The potential ψ then satisfies the two-dimensional Poisson equation

$$\frac{\partial^2 \psi}{\partial \theta_{I1}^2} + \frac{\partial^2 \psi}{\partial \theta_{I2}^2} = \frac{8\pi d_{OL}d_{LS}\Sigma}{d_{OS}} = \frac{2\Sigma}{\Sigma_c}, \quad (2.5)$$

where the derivatives are with respect to Cartesian axes in the image plane. The quantity Σ_c is the critical density at which a uniform sheet of matter would just focus radiation from the source at the observer (e.g., Turner, Ostriker, and Gott 1984).

The total time delay is obtained by adding the geometrical and gravitational contributions. In these cosmologically scaled units,

$$\tau(\theta_I; \theta_S) = \frac{1}{2}(\theta_I - \theta_S)^2 - \psi(\theta_I), \quad (2.6)$$

where $\tau(\theta_I; \theta_S)$ is the time surface. By Fermat's principle, for a given source position θ_S , the images are located at the stationary points of $\tau(\theta_I; \theta_S)$ with respect to variations of θ_I . In the absence of intervening mass, $\tau(\theta_I; \theta_S)$ is simply a paraboloid and the single image is located at the minimum, $\theta_I = \theta_S$. As mass is gradually introduced (with $\psi < 0$) the arrival-time surface will be raised and new extrema will eventually be created (maxima, minima, and saddle points) corresponding to new images. Figure 2 shows a typical sequence of contour plots with increasing lens mass.

The condition $\partial\tau/\partial\theta_I = 0$ satisfied by the images gives

$$\theta_I = \theta_S + \nabla\psi(\theta_I) = \theta_S + \alpha'(\theta_I), \quad (2.7)$$

where α' is related to the deflection angle α in Figure 1 as follows:

$$\alpha'(\theta_I) = \frac{d_{LS}}{d_{OS}} \alpha(\theta_I). \quad (2.8)$$

Equation (2.7) recovers the standard vector equation (Bourassa and Kantowski 1975), thus demonstrating the equivalence of the vector and scalar approaches. This equation can also be written in the following alternate form:

$$\theta_S = \nabla\tau(\theta_I; 0). \quad (2.9)$$

Thus, a single time surface, corresponding to $\theta_S = 0$, suffices to describe lensing by a given mass distribution for any source position (at fixed redshift z_S).

Now consider the scaled (extrinsic) curvature tensor

$$K_{ij} = \tau_{,ij} = \delta_{ij} - \frac{\partial^2 \psi}{\partial \theta_{Ii} \partial \theta_{Ij}} = \frac{\partial \theta_{Si}}{\partial \theta_{Ij}}. \quad (2.10)$$

K_{ij} is also the Hessian of the transformation $\theta_I \rightarrow \theta_S$. The mapping from the source plane to the image plane is described by the magnification tensor $M_{ij} = K_{ij}^{-1}$. Let us now rotate the

coordinate system on the sky in order to diagonalize the curvature tensor K_{ij} at the position θ_I . In these special coordinates,

$$K_{ij} = \begin{bmatrix} 1/\rho_1 & 0 \\ 0 & 1/\rho_2 \end{bmatrix}, \quad (2.11)$$

where ρ_1, ρ_2 are the principal radii of curvature of the time-delay surface. The total magnification is given by the Jacobian for the transformation $\theta_S \rightarrow \theta_I$:

$$M = |M_{ij}| = \rho_1 \rho_2. \quad (2.12)$$

Thus the magnification increases with decreasing Gaussian curvature. We write the diagonalized curvature tensor in the form

$$K_{ij} = \begin{bmatrix} \kappa + \mu & 0 \\ 0 & \kappa - \mu \end{bmatrix}, \quad (2.13)$$

where $\kappa = \frac{1}{2}(\rho_1^{-1} + \rho_2^{-1}) = 1 - \Sigma/\Sigma_c$ is the *expansion* and $\mu = \frac{1}{2}(\rho_1^{-1} - \rho_2^{-1})$ is the *shear*. In terms of this decomposition, the magnification of the image is given by

$$M = (\kappa^2 - \mu^2)^{-1}. \quad (2.14)$$

We can use the eigenvalues of the magnification tensor, ρ_1, ρ_2 , to classify the parity of the image. The *partial parities* of the image are defined to be equal to the signs of the two eigenvalues, and the *total parity* is the sign of the product of the eigenvalues. Thus, at a *minimum* of the time surface, the partial parities are both positive and so is the total parity. A *maximum* has negative partial parities and positive total parity, while a *saddle point* has negative total parity and partial parities of opposite signs. Figure 3 interprets the standard bending angle diagram for a circularly symmetric lens (e.g., Young *et al.* 1980) in terms of the parities of the images and the nature of the extrema (see also Narayan, Blandford, and Nityananda 1984).

At this point we should clarify what properties of the source can be inferred in principle from observations of the images. Let us define a resolved image as one in which three or more noncollinear points can be clearly identified (as in a bent jet). (We assume that the source is not so extended that the different images overlap.) If the image is sufficiently small compared with the scale of the underlying potential, then its shape should be related to that of the source by a translation plus a transformation tensor (cf. Narayan, Blandford, and Nityananda 1984; Gorenstein *et al.* 1984; see also Blandford and Jarošzyński 1981, who considered the opposite limit where a small lens introduces a local kink in a long, straight jet). If the lens is localized at a specific redshift and is described by a scalar potential (as, for example, would not be true of a moving string), then each source-to-image transformation tensor is symmetric (cf. eq. [2.10]). In other words, the image is expanded and sheared, but not rotated.

However, the transformation from source to image is not directly observed. What can be determined is the transformation tensor between two resolved images. Given the coordinates of three identified points in both images, or some equivalent model fitting (cf. Gorenstein *et al.* 1984), we can solve directly for all four elements in each image-to-image transformation tensor. This tensor will not, in general, be symmetric. Now suppose that we resolve n images and can therefore determine $(n-1)$ four-element image-to-image transformation tensors. One element in each tensor can be associated with an essentially unconstrained magnification.

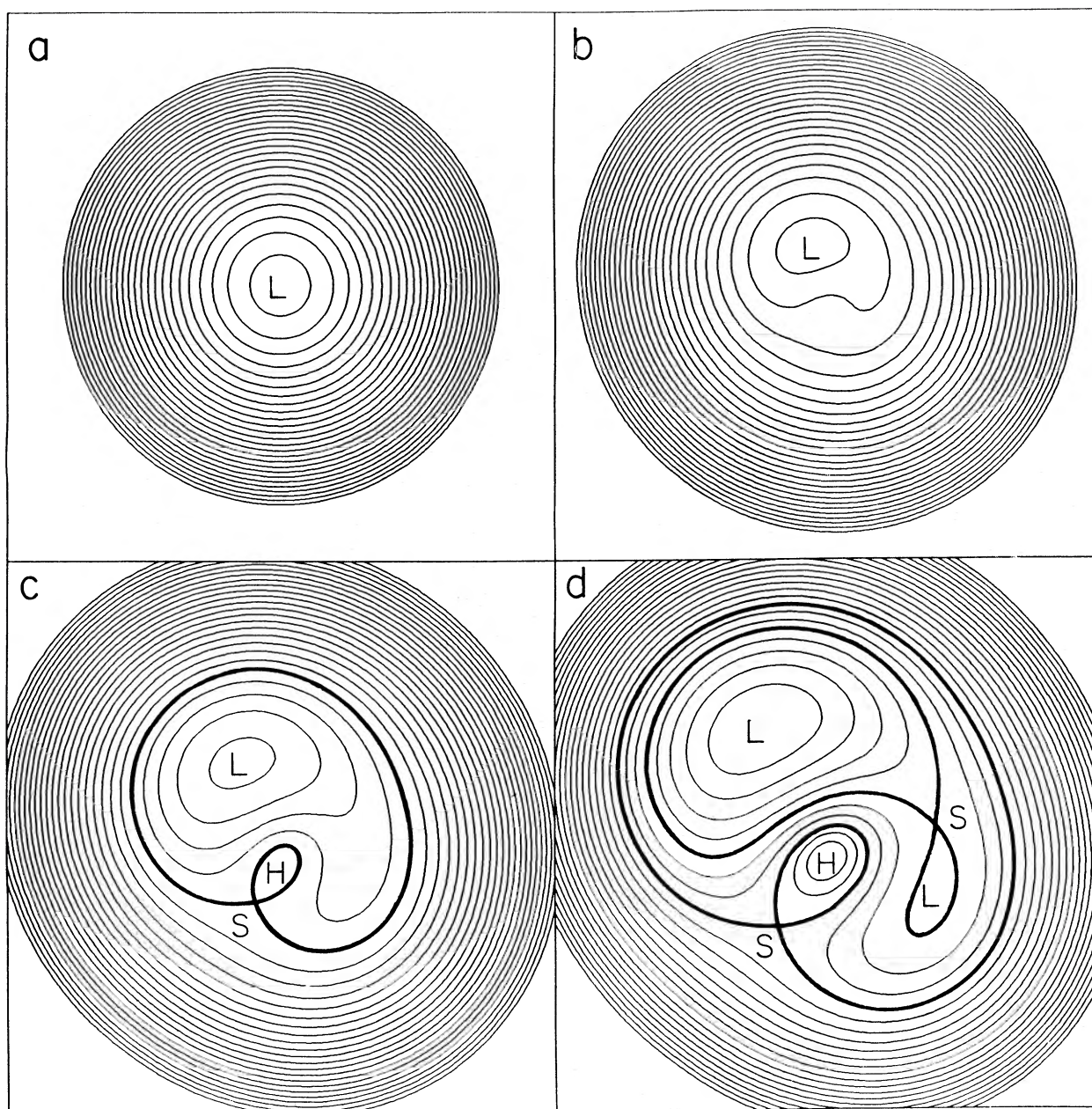


FIG. 2.—Contours of arrival time $\tau(\theta_l; \theta_s)$ in the θ_l plane for a simple elliptical galaxy lens in which the surface density (or, equivalently, the distance d_{OL}) is increased. The source is located at the centers of the four diagrams. (a) When the lens is absent, the contours are circular and the image is located at the central minimum (L). (b) When the surface density is 1 unit, the contours are distorted but there is still only one image. (c) When the surface density is increased to 2 units, a maximum (H) and a saddle point (S) are created, giving a total of three images with a limaçon topology (cf. Fig. 5b). (d) At a larger surface density (3 units), the existing minimum will split into two minima and another saddle point with lemniscate topology (cf. Fig. 6c).

We may, however, solve for the remaining $2n$ unknown source-to-image transformation tensor elements using the $3(n-1)$ known image-to-image transformation tensor elements. This can be done uniquely if $n=3$, and we can infer the source shape up to an unknown scale factor. If there are more than three resolved images, then the solution is overdetermined and we have a check on the underlying assumption that the lens is well described by a smooth, stationary mass distribution localized in redshift.

If, as is currently true for Q0957+561, we only resolve two images, then we can still tell whether or not one of the images is a saddle point, since, if this is so, the determinant of the image-

to-image transformation tensor will be negative. If we believe that neither image is a saddle point (for example, if the determinant of the image-to-image transformation tensor is positive and we believe that there are only three images), then we can distinguish a maximum-minimum combination from either a maximum-maximum or a minimum-minimum combination by inspecting the sign of the trace of the image-to-image transformation tensor, which will be negative for the maximum-minimum case.

In this context, it is worth noting that the polarization position angle will be unchanged by the gravitational deflection, and this provides a further possible confirmatory test of gravi-

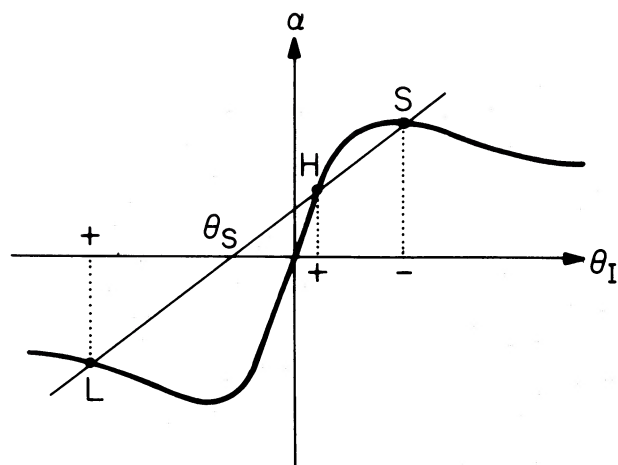


FIG. 3.—The thick line shows the bending angle α as a function of impact parameter θ_I for a typical circularly symmetric lens. The sloping straight line intercepts the abscissa at the location of the source θ_S . The intersections of these two lines give the locations of the three images (e.g., Young *et al.* 1980). The parities +, − and the nature of the extrema in the time surface, L for low, H for high, and S for saddle point, are indicated. This geometry corresponds to the limaçon discussed in § III and shown in Fig. 5b.

tational lens action. Furthermore, if we believe that the position angle of the polarization direction in a radio jet is related to the direction of the jet (cf. Rusk and Seaquist 1985), then polarization observations can give a direct determination of the orientation of the source.

Using Fermat's principle and the topology of the time surface, we can now make the following general statements:

1. Provided that there are no discontinuities in the time surface (that is to say, we have a nonsingular, transparent potential), there is always an odd number $2n + 1$ of images, of which $n + 1$ have positive total parity and n have negative total parity (cf. Burke 1981). This is obvious in terms of the time surface because there is one positive-parity image in the absence of the lens and the addition of the lensing mass produces new images in pairs of opposite parity. The odd-number theorem is of course not valid if there are singularities in the lens, as with black holes or strings, or if there is obscuration of images.

2. If one could measure the relative arrival times of the images (which should be possible for a variable source), then the earliest image will always have positive partial parities and hence positive total parity. This is because the time delay goes to $+\infty$ for large $|\theta_I|$, and therefore the image with the least time delay has to be a global minimum. In other words, the first image to vary must have the majority parity. This result, which holds for an arbitrary (odd) number of images, and even with multiple lens planes (cf. § VI), means that if ever one finds the earliest image to have negative parity, then one can be certain that some images have been missed.

3. Images with positive partial parities (of which there is always at least one by statement 2 above) each contain more flux than the original source (Schneider 1984). To prove this, we consider the representation of the curvature matrix given in equation (2.13). Using equation (2.5), the convergence κ is given by

$$\kappa = 1 - \Sigma/\Sigma_c. \quad (2.15)$$

Thus κ depends only upon the matter along the line of sight

and must be less than unity.¹ The shear term μ arises from matter outside the beam and is in general nonzero. The partial parities are the signs of $\kappa + \mu$ and $\kappa - \mu$. When they are both positive, we have $|\mu| < \kappa < 1$, which implies through equation (2.14) that $M > 1$.

4. Images with negative partial parities (maxima in the arrival-time surface) are created by rays that pass through a mass density in excess of the critical density Σ_c . To see this, note that if both partial parities are negative, then $\partial^2\psi/\partial\theta_{I1}^2 > 1$ and $\partial^2\psi/\partial\theta_{I2}^2 > 1$, which implies that $\Sigma > \Sigma_c$ from equation (2.5). Likewise, a minimum must have $\kappa > 0$ and from equation (2.15) must be located at a point of subcritical surface density. There is no bound of either sign on the density necessary to produce a saddle point. Interestingly enough, one can have multiple images even when Σ does not exceed Σ_c anywhere on the sky. Since there can be no maxima in such cases, the image topologies (§ III) and parities are restricted (only Figs. 4b and 6a are permitted among the topologies considered in this paper).

5. Images which are closer together tend to be brighter than isolated ones and the flux goes to infinity as the images merge. In fact, an isolated image cannot become arbitrarily bright except in nongeneric high-symmetry geometries or in the vicinity of a cusp or higher order catastrophe. We amplify this in our discussion of catastrophe theory in § V.

6. If we only see two out of three images because of a singularity in the gravitational potential, then the nature of this singularity may be elucidated by studying the parities of the observed images. A black hole singularity will produce two images of opposite total parity, whereas a string will give images of similar parity. This becomes clear from the discussion of § III and Figures 4 and 5. The “missing” image cannot have both partial parities positive.

We are also interested in calculating the cross section for lensing of a quasar at redshift z_S by a lens at redshift z_L . This is much easier to compute by integration over the image plane than over the source plane. The cross section for a point source to undergo some lensing event is given by

$$\sigma = \int d^2\theta_S = \int |M|^{-1} d^2\theta_I, \quad (2.16)$$

where we have used the fact that $|M|$ is the Jacobian relating the two spaces. In evaluating the second integral in equation (2.16), we must be careful to include just one image per source position because of the one-to-many mapping from θ_S to θ_I .

We have assumed that the lensing mass distribution is localized in the sky, so that far from the lens the spacetime tends asymptotically to that of the background isotropic universe. This is of course true for most lenses of interest. However, if we consider lensing by infinitely long strings (Vilenkin 1984; Gott 1984; Hogan and Narayan 1984), this is not strictly valid because spacetime takes on a “conical” character. For many purposes we can still replace the string by a Newtonian mass density along a line and use the corresponding linear potential. However, it must be remembered that a string that is tilted by

¹ The statement that the surface density Σ is positive is not strictly true. For example, consider an Einstein–de Sitter cosmology with a spherical void in the lensing plane subtending an angle $\theta_v \ll 1$. This will contribute an effective negative surface density $\Sigma \sim -\theta_v \Sigma_c$ (cf. Nityananda and Ostriker 1984). However, provided that there are not significant deviations from mean cosmological density along the line of sight, and this assumption underlies our single-screen model, the surface density can never become sufficiently negative to affect the lensing geometry strongly.

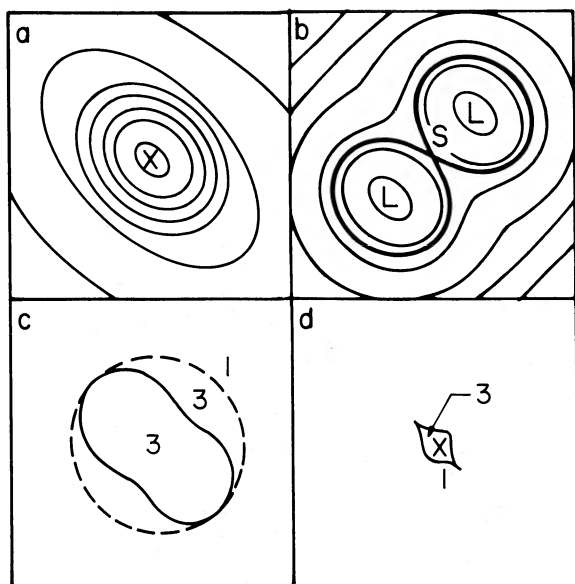


FIG. 4.—(a) Contours of projected density of a model galaxy lens with an elliptical shape. The density has been adjusted so that rays from the source are focused in front of the observer in a plane that runs from the lower left-hand corner to the upper right-hand corner of the diagram, but behind the observer in a perpendicular direction, i.e., the lens is astigmatic. A limiting case of this type of lens is a straight string, which only focuses in one direction. (b) Contours of time delay for the given source located at X , computed as discussed in § IV. The contour spacing has been selected to highlight the three extrema, consisting of two L (low) images and one S (saddle point) image. The “critical” contour passing through S is highlighted, and distinguishes the topology (*lemniscate* in this case) of the lensing. If the lens were a string, S would lie on the string and have zero magnification. The remaining images will have the same (viz., positive) parity. (c) The solid line shows the caustic in the image plane (θ_I), which is the locus of points at which an L and an S image merge with infinite amplification and then disappear in a fold catastrophe. The S image always lies inside this closed curve, and the L images outside. The dashed line shows the location of the third image when the other two merge. Multiple images are always found inside this curve. The two points at which the solid and dashed lines meet are cusp catastrophes (positive cusps; see § V), involving the simultaneous merger of all three images. (d) Shows the caustic curve in source space (θ_S), consisting of two cusps joined by two smooth curves of fold catastrophe. Multiple images are produced only when the source is inside the curve. The detailed structure of a cusp caustic is discussed in § V and Fig. 9.

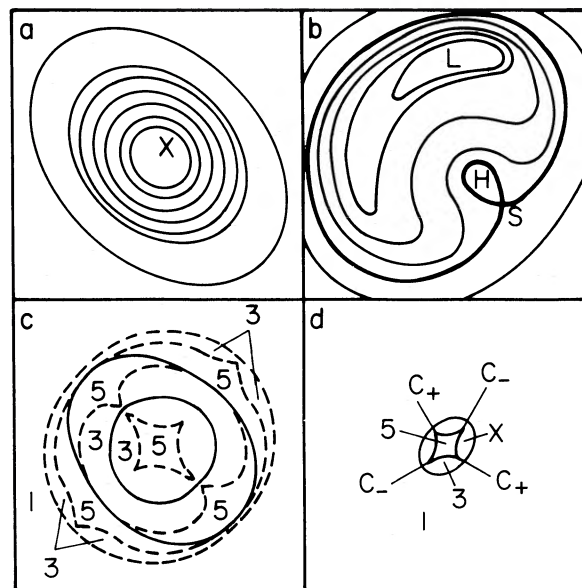


FIG. 5.—(a) Contours of projected density of an elliptical lens corresponding to a case when rays from the source are focused in front of the observer in both principal directions. A limiting case of this type of lens is a point mass, say a black hole. (b) Contours of time delay corresponding to the source at X , computed as discussed in § IV. The three extrema consist of an L (low) image, an H (high) image and an S (saddle point) image. The critical contour has the shape of a limaçon. If the lens were a black hole, H would lie on the singularity with zero magnification and the surviving images would have opposite parities. (c) The inner solid line shows the caustic corresponding to the transition from three images to one image, involving the merger and disappearance of the H and S images. The outer solid line is a second caustic, involving the transition from three to five images and must always be present, as discussed in the text and also shown in Fig. 10. There are two positive cusps C_+ and two negative C_- on this caustic (see § V for the distinction between positive and negative cusps). The dashed lines demarcate areas on the image plane corresponding to one, three, and five images. (d) The two caustics in the source plane. The outer curve is a pure fold corresponding to the transition from one to three images. The inner curve consists of four cusps joined by folds and corresponds to the transition from three to five images. The topology of the time surface in the five-image region is shown in Fig. 6c. When the lens is made perfectly circular, as in the case discussed in Fig. 3, the inner caustic in (d) shrinks to a point, thus corresponding to a nonstandard, nongeneric catastrophe. The corresponding caustic in the image plane (c) is, however, topologically unaffected, in the sense that it is still a finite closed curve.

an angle φ from the plane of the sky has a *reduced* bending proportional to $\sin \varphi$, a somewhat surprising result that arises from the peculiar nature of the spacetime (Gott 1984).

Let us summarize this section. We assume that there is a lensing mass in between us and the source. We calculate the two-dimensional Newtonian potential in the lens plane using the integral form of Poisson's equation and convert it into an effective relativistic potential. We compute the arrival times for possible rays passing through the lens plane and locate the actual observed images by the extrema of these arrival times. The associated magnifications and parities of the images are given by the curvature tensor of the arrival-time function at these extrema.

III. TOPOLOGICAL CLASSIFICATION OF IMAGE CONFIGURATION

It is by now quite clear that the geometries in the observed examples of gravitational lensing are not simple, and we must probably renounce hope of using the observations to make quantitative estimates of the masses of galaxies or the value of the Hubble constant (e.g., Falco, Gorenstein, and Shapiro

1984; Alcock and Anderson 1984). Nevertheless, we may be able to understand the imaging geometry in qualitative, topological terms.

In the absence of a lens, the time-delay function $\tau(\theta_I; \theta_S)$ is just a paraboloid centered on the source. The effect of adding masses in the lens plane is to raise this surface in the region around the mass. If the mass is large enough, then we will create new extrema with associated images.

Let us first consider three-image topologies. We represent maxima (highs), minima (lows) and saddle points on the time surface by the symbols H , L , and S . By the discussion in § II, one of the three images has to be S and one L . Therefore, there are only two possible three-image topologies— LLS and LHS . These are shown in Figures 4b and 5b, where we have emphasized the “critical” isochronal contours passing through the saddle points. The shapes of the critical contours in the two cases are those of the classical *lemniscate* and *limaçon* curves, and we will use these terms henceforth. The usual example, discussed in the literature, of three-image lensing by a (spherical) galaxy with a non singular core (Fig. 3) corresponds

to the limaçon. The lemniscate does not appear to have been distinguished so far. It occurs naturally with elongated lenses as shown in Figure 4. It is also more likely to be produced when the mass distribution in the lens is extended rather than centrally concentrated.

If we consider holding the lens fixed and moving the source around, the images and the critical contour will also move. For particular source positions, two of the images will merge and disappear in a caustic singularity. This is shown for the case of the lemniscate by the solid line in Figure 4c. The dashed line shows the location of the third image at the instant when a pair merges at the caustic. The significance of this line is that, whenever an image is found outside it, it is the only image. That is, three-image geometries have all three images inside this line. There are two points at which the caustic and single-image curves in Figure 4c touch. These correspond to cusp catastrophes where three images simultaneously merge into one. This is to be contrasted with the fold catastrophe which occurs over the rest of the caustic, where only two images merge. Figure 4d shows the shape of the caustic in the source plane. Caustics are discussed in detail in § V.

The case of the limaçon in Figure 5b is a little more complicated. We still have a caustic separating one- and three-image geometries, shown by the inner of the two solid lines in the image plane (Fig. 5c). However, the generic limaçon-producing lens must possess a second caustic, shown by the outer of the two solid lines, corresponding to a transition from three to five images. A very general topological argument can be made to show this. Consider moving the source from left to right in the figure. At far left one has only one *L* image. As the source moves to the right, at one point a pair of images is created and we have the configuration *LHS* as in Figure 5b. Still later, as the source moves to the far right, we again have only one *L* image. For certain trajectories of the source, the *H* and *S* images will merge, leaving the original *L* image as the survivor. A little thought, however, shows that this cannot happen for all trajectories. In fact, for certain "central" trajectories, we will require the *L* and *H* images to merge, which is impossible without creating additional images. Similarly, the *S* must turn into *L*, which also requires additional images. Thus there must be a region of five or more images (cf. Figs. 5 and 10). The only way to avoid this topological argument that insists on five images is to have a very special lens distribution where *L* and *S* combine into a single closed trench in the time-delay surface of constant τ (a Mexican hat with a level bottom). This leads to a ringlike image for a particular position of the source. In a sense, the caustic is still there, except that the whole caustic is lighted up for a single source position. (One could also argue that this is a case of an infinite number of images.) Turner, Ostriker, and Gott (1984) have studied amplifications and cross sections for this special case, using a circularly symmetric lens. However, it is clear that this geometry cannot occur in practice, since any random mass distribution far away from the beam will introduce shear into the local curvature tensor, breaking the symmetry. Nityananda and Ostriker (1984) and Hogan and Narayan (1984) have studied the effect of the shear in specific cases, and find that one generally has a region of parameter space with five images. As shown in Figure 5d, the one- to three-image caustic in source space (*outer solid line*) is a pure fold catastrophe, while the three- to five-image caustic (*inner solid line*) has cusp catastrophes in addition (four cusps in this case).

The lemniscate and the limaçon are basic building blocks for

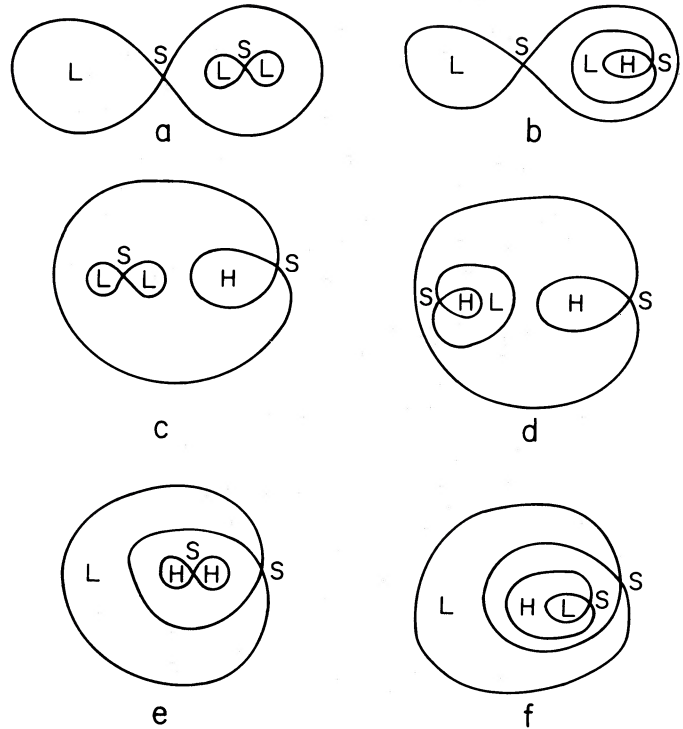


FIG. 6.—(a-f) The six topologically distinct five-image arrangements possible. Types (b) and (f) cannot have cusp catastrophes, as discussed in § V.

the critical contour plots when five or more images are formed. In Figure 6 we give the six possible nondegenerate topological possibilities for five images. There are 25 topologically distinct nondegenerate arrival-time surfaces containing seven images. Our definition of "degenerate" here is that two or more saddle points have a common isochronal contour or that two images merge. If we change the image topology by continuously altering the potential, then we must pass through one of these degenerate configurations.

In a given case of lensing, it may be possible to determine the parities of all the images, using, say, VLBI. In addition, it may also be possible to measure relative time delays, thus permitting the images to be time ordered. These two pieces of information uniquely determine the topology in the three-image case, as shown in Table 1. Note that the negative-parity image cannot arrive earliest, as discussed in § II. In the case of five images, there are six permitted types of time ordering and four forbidden (Table 1). Of the permitted types, only two correspond to a unique topology. Even in the other four nonunique cases, it could happen that pairs of opposite-parity images are brightened and appear close to each other in the sky, in which case it would be natural to interpret them as merging pairs. This will uniquely determine the topology.

IV. INTERACTIVE USE IN INTERPRETATION OF OBSERVATIONAL DATA

Fermat's principle can be applied to the practical problem of finding simple lens geometries that reproduce given observed image configurations. We have written a routine to compute the two-dimensional potential ψ , and hence the arrival time for a given source position, due to a given distribution of mass on the sky. The images are located at the extrema of the arrival time surface, and the associated magnifications, and shapes of

TABLE 1
IMAGE PARITIES

Parities of Time-ordered Images	Topology (Figure Number)
++-	4b
+ - +	5b
- + +	...
+++--	6a
++-+-	6a, 6b
+ + - +	6b, 6c, 6f
+ - + +	6b
+ - + - +	6b, 6d, 6f
+ - - + +	6d, 6e
- + + + -	...
- + + - +	...
- + - + +	...
- - + + +	...

NOTE.—The first column gives the parities of the images in sequence of arrival times, the earliest image being listed first. The second column lists the topologies that can give rise to the particular ordering. Orderings with the earliest image having negative parity are not allowed.

extended images, are given by the local curvature tensor. We have developed a computer-graphical package which plots the isochronal contours on a TV screen. This is a great help in interactively fine-tuning the parameters characterizing the mass distribution of the lens so as to reproduce a wide variety of image configurations. The effect of adding or subtracting mass is to increase or decrease the function $\tau(\theta_l)$ locally and thus to alter the image locations and magnifications in a manner which is easy to appreciate. As Figure 7 shows, an additional mass M attracts/repels images parallel to negative/positive curvature principal axes, the forces being proportional to $M/(|\theta_M - \theta_l|)$ and to the respective radii of curvature.

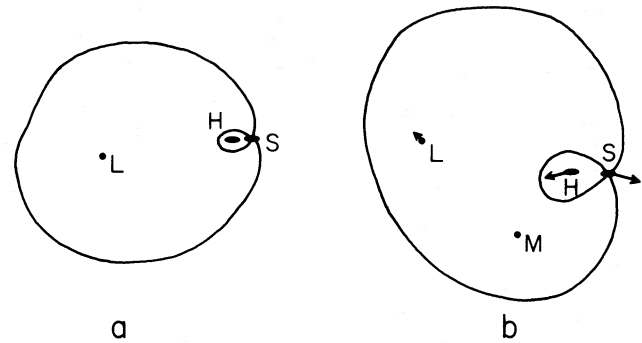


FIG. 7.—(a) Schematically shows a limaçon topology with three images, L , H , and S . (b) Shows the effect of adding an additional point mass M . This repels the image at L , attracts the one at H , repels S along the direction HS and attracts it along the perpendicular direction. The magnitudes of the response depend on the strength of M , the distance between M and the image, and the values of the local principal radii of curvature of the time surface.

Figures 4 and 5 were made using this computer routine. We have also reproduced the six five-image topologies of Figure 6 using positive mass distributions. (There is no guarantee that there exist inversions of given image distributions that satisfy this physical constraint.) Applications of this computer routine to the modeling of observed cases of gravitational lensing and the estimation of cross sections for various types of lenses and lensing events will be discussed in a separate publication.

In fact, there is an alternative to the computer-graphical approach, which has some heuristic value. It is possible to construct an optical analog device (although we have not actually carried this out) that simulates gravitational lensing. One possible design is shown in Figure 8. A reflecting elastic membrane (e.g., silvered Mylar) is fitted around a circular frame. Light from a source above passes through a half-silver mirror and is reflected by the membrane. The reflected rays are bent by the mirror before being focused by a lens system to

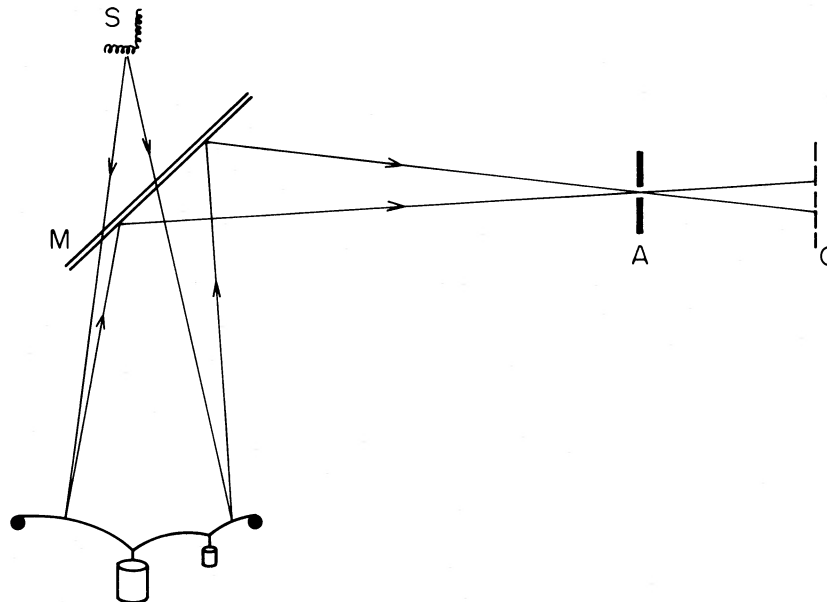


FIG. 8.—Schematic design of a gravitational lens simulator. S is a bright light source with an asymmetric shape to permit determination of image parities, M is a half-silvered mirror, and L is the “lens,” simulated by means of a reflecting elastic membrane deformed by hanging weights or blowing air jets. The source can be observed visually through a small aperture, A , or can be reimaged onto a screen, C .

produce a real image on a screen. In the case of an undeformed membrane, there will be one spot of light on the image screen, corresponding to the single minimum in the geometric time surface $t_{\text{geom}}(\theta_I; \theta_S)$. A gravitational lens can now be simulated by hanging proportionate weights from the bottom of the membrane or (more practically) by blowing high-pressure air jets at it. As long as the displacement $z(r)$ of the membrane is small, it satisfies the two-dimensional Poisson equation

$$\nabla^2 z = \Sigma(r)g/\tau, \quad (4.1)$$

where $\Sigma(r)$ is the surface density of the mass distribution, g is the acceleration due to gravity, and τ is the surface tension of the membrane. Since the light propagation time depends linearly on z , Fermat's principle works in this analog device exactly as in the real lensing situation (compare with eqs. [2.5] and [2.6]). As the membrane is pulled down by the hanging masses, new extrema will be created, which will appear as additional spots on the screen. The brightness of these spots will correspond directly to the magnification of the associated images, and their parity can be monitored if the light source has a finite size and an asymmetric shape. Displacements of the source and the viewing screen can be used to simulate variations in θ_S , z_S , and z_L . The parameters of the lens can be tuned by changing the air jets.

V. CATASTROPHE THEORY AND THE MERGING OF IMAGES

We have shown how different types of lenses give rise to topologically distinguishable arrival-time surfaces. We now consider the details of the transition from one topology to another through the merger/creation of pairs of images. In the language of catastrophe theory, the position on the sky of the source (keeping the redshift fixed) gives us two control variables $(x_S, y_S) \equiv \theta_S$ in Cartesian coordinates referred to a suitably selected origin. The arrival time for a given θ_S is a function of two coordinates $(x_I, y_I) \equiv \theta_I$ (known in catastrophe theory as state variables) on the sky in the image plane. We are interested in the change in the topology of the arrival-time surface as we alter the control variables.

If the source is in a direction well away from the lens, then there will be just one image, and the isochronal contours are a set of nested curves that are topologically equivalent to circles. If the lens is strong enough, then, as we move the source closer to the lens, a stage will come when a pair of images will be created, thereby changing the shape of the arrival-time contours. As discussed in § III, the critical contour that passes through the saddle point takes the form of either the lemniscate or the limaçon. The line in the control (i.e., source) plane across which this change occurs, which may be located through the vanishing of the determinant of the curvature tensor K_{ij} , is a caustic (or catastrophe). Correspondingly, there is a line in the state variable space on which images merge (or are created) (cf. Figs. 4 and 5). For simplicity, we will also refer to this line as a caustic. For two control variables, there are two possible elementary catastrophes (e.g., Poston and Stewart 1978; Berry and Upstill 1980) known as the *fold* and the *cusp*, both of which can occur.

Before discussing the properties of these catastrophes in detail, let us first fix ideas by considering the mapping between the source and image planes when there is only one isolated image. If we choose the origin in the two spaces such that a source located at $\theta_S = 0$ gives an image at $\theta_I = 0$, then, for

suitably oriented Cartesian axes, the time surface locally takes the form

$$\tau(\theta_I) = \frac{1}{2}ax_I^2 + \frac{1}{2}by_I^2 + \cdots, \quad (5.1)$$

where we have ignored an additive constant. The constants a , b can be expressed in terms of the derivatives of the potential ψ by expanding equation (2.6) in a Taylor series. Positivity of the surface density implies that $a + b \leq 2$. The position of the image for a general θ_S is given by equation (2.9) as

$$x_I = \frac{1}{a}x_S, \quad y_I = \frac{1}{b}y_S. \quad (5.2)$$

The mapping between the two planes is seen to be a simple stretching by factors of $1/a$ and $1/b$ parallel to the two coordinate axes. A circular source is thus mapped into an ellipse, with a magnification given by

$$M = \frac{1}{ab}. \quad (5.3)$$

It should be stressed that equation (5.1) is a *local* expansion of the time surface. The *global* time surface could well have other extrema, with associated images, far from the region of validity of this expansion.

In the case of the fold catastrophe, the time surface is locally of the form

$$\tau(\theta_I) = \frac{1}{3}ax_I^3 + \frac{1}{2}bx_I^2 + (bc)^{1/2}x_I y_I + \frac{1}{2}cy_I^2, \quad (5.4)$$

where $a > 0$ without loss of generality. Note that this form is more general than the canonical catastrophe function (e.g., Poston and Stewart 1978). Now the image locations are given by

$$x_I = \pm \frac{1}{a} \left[x_S - \left(\frac{b}{c} \right)^{1/2} y_S \right]^{1/2}, \quad y_I = \frac{1}{c} y_S - \left(\frac{b}{c} \right)^{1/2} x_I, \quad (5.5)$$

and the magnification of each image is

$$M = \frac{1}{2acx_I} = \frac{1}{2a^{1/2}c[x_S - (b/c)^{1/2}y_S]^{1/2}}. \quad (5.6)$$

The new feature is that, for $x_S > (b/c)^{1/2}y_S$ there are two images, while for $x_S < (b/c)^{1/2}y_S$ there are no images (though globally, of course, there must in both cases be at least one other image in order to satisfy the odd-number theorem). When $x_S = (b/c)^{1/2}y_S$, the two images merge at $x_I = 0$ with infinite amplification. The direction of merger is given by $dy_I/dx_I = -(b/c)^{1/2}$. The lines $x_I = 0$ and $x_S = (b/c)^{1/2}y_S$ thus represent the caustic in the two planes. (Although the expansion [5.4] leads to a caustic that is locally a straight line, for any finite lens it must globally form a closed non-self-intersecting loop.) The two merging images approach each other from opposite sides of the caustic and hence by equation (5.6) have opposite parities. Both limaçons and lemniscates can have fold catastrophes.

For the cusp catastrophe, the local time surface is of the form

$$\tau(\theta_I) = \frac{1}{4}ax_I^4 + \frac{1}{2}bx_I^2 y_I + \frac{1}{2}cy_I^2. \quad (5.7)$$

The images are located at the solutions of the equations

$$ax_I^3 + bx_I y_I = x_S, \quad \frac{1}{2}bx_I^2 + cy_I = y_S, \quad (5.8)$$

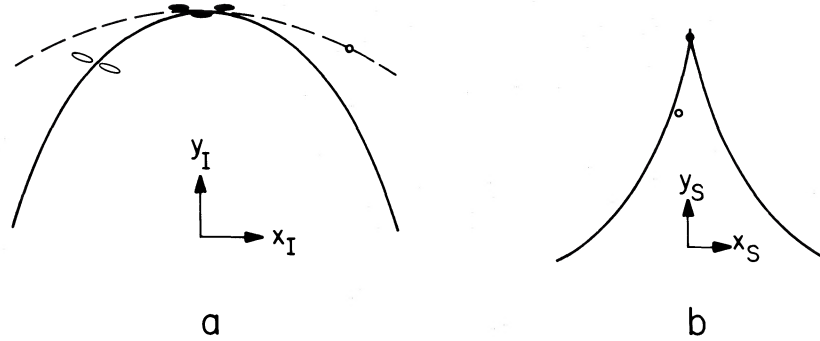


FIG. 9.—Cusp caustic in image plane (a) and source plane (b). The case displayed corresponds to a positive cusp. The solid ellipses show the locations and shapes of the images when the source is very close to the cusp [solid circle in (b)]. The three images merge simultaneously along a direction tangential to the caustic when the source is exactly on the cusp, and for a source just outside the cusp there is only one very bright image. Away from the cusp, the caustic in (b) behaves like a fold. As shown by the open circles and ellipses, when the source approaches and crosses the caustic line in this region, two bright elongated images merge and disappear, while the third unbrightened image crosses the dashed single-image line. See Hogan and Narayan (1984) for a pictorial description of the fold caustic.

and the magnification is

$$M = \frac{1}{(3ac - b^2)x_I^2 + bcy_I}. \quad (5.9)$$

The caustic, which is given by the condition $M \rightarrow \infty$, is of the form

$$y_I = \left(\frac{b^2 - 3ac}{bc} \right) x_I^2 \quad (5.10)$$

in the image plane, and of the form

$$y_S^3 = \frac{27c^2}{8b} \left(1 - \frac{2ac}{b^2} \right) x_S^2 \quad (5.11)$$

in the source plane. Note the characteristic three-halves power relation in the source plane, illustrated in Figure 9. For source positions “inside” the cusp caustic in the source plane, there are three images, and for positions “outside” only one. When $\theta_S = 0$, the three images merge simultaneously at $\theta_I = 0$, leaving behind one infinitely brightened image at the same location. In the time surface, three extrema coalesce and the critical contour shrinks to a point. As the cusp is approached, the images become elongated parallel to the caustic in the image plane. Note that a cusp caustic (or higher order catastrophe, if there were more than two control variables) is the only way to produce an *isolated*, highly magnified image—a fold caustic is not enough. For other positions of the source on the source caustic (5.11), two images merge at a corresponding point on the image caustic (5.10), leaving behind a single not-so-bright image. The locus of this single image when the other two images merge is given by

$$y_I = -\frac{(b^2 + 6ac)}{8bc} x_I^2, \quad (5.12)$$

and its magnification is

$$M = [4(ac - \frac{1}{2}b^2)x^2]^{-1}. \quad (5.13)$$

Two types of cusp caustic can now be distinguished:

1. *Positive cusp*: When $b^2 < 2ac$, two positive-parity images and a saddle point merge to leave behind a positive-parity image. The positive-parity images are both minima (maxima) if $a, c > 0$ ($a, c < 0$). This type of cusp is produced by the shrinking of a lemniscate and takes place only in the topologies of Figures 5b, 6a, 6c, and 6e. The limaçon of

Figure 5b cannot have a cusp in the one-to-three image caustic. However, since the generic limaçon-producing lens has a region of five images (Figs. 5 and 10), there will be cusps associated with the three-to-five image caustic.

2. *Negative cusp*: When $b^2 > 2ac$, one positive-parity image and two negative-parity saddle points merge to leave behind a saddle point. The positive-parity image is a minimum (maximum) if $c > 0$ ($c < 0$). Since this configuration involves two saddle points, it requires the presence of at least five images. Also, since at the cusp the three images have the same value of τ , the critical isochronal contours are *degenerate* in the sense that the same contour passes through both saddles. Negative cusps can form in the topologies of Figures 6a, 6c, 6d, and 6e.

The caustic in Figure 4d contains two positive cusps. The inner caustic in Figure 5d contains two positive and two negative cusps.

The importance of caustics is that images in their vicinity are highly magnified and so could dominate flux-limited samples (this so-called amplification bias was emphasized by Turner, Ostriker, and Gott 1984). Both the fold and the cusp have the property that the magnification of an image at a perpendicular distance Δr_I from the caustic line in the image plane scales asymptotically as

$$M \propto \frac{1}{\Delta r_I}. \quad (5.14)$$

The coefficient is sensitive to the model but is typically of the order of the critical impact parameter for multiple imaging. The asymptotic, integral cross section for producing pairs of images, each with magnification in excess of some absolute value $M_0 \gg 1$, is given using equation (2.16) by

$$\sigma(|M| > M_0) = \frac{1}{2} \int d^2\theta_S = \frac{1}{2} \int \frac{d^2\theta_I}{M}. \quad (5.15)$$

The factor of $\frac{1}{2}$ is introduced in the second integral to include only one image per source position. Introducing a local coordinate system parallel and perpendicular to the caustic (where $|M| \rightarrow \infty$) and using equation (5.14), the surface integral is transformed into a line integral:

$$\sigma(|M| > M_0) = \frac{1}{2M_0^2} \oint_{K=0} \frac{|d\theta_I \times \nabla_I K|}{|\nabla_I K|^2} \propto \frac{1}{M_0^2}, \quad (5.16)$$

where $K = |K_{ij}| = 1/M_0$ (cf. eq. [2.10]), and the integral is performed along all caustics, i.e., curves with $K = 0$. In the case of the cusp, there is some cross section for producing three comparably bright images. However, it turns out that this cross section falls off as a higher power of the magnification than the cross section for producing just two comparably bright images. We are therefore justified in regarding equation (5.16) as asymptotically valid even in the presence of cusps, or indeed higher order catastrophes.

If the sources that are being lensed have a luminosity function

$$\phi(L > L_0) \propto L_0^{-\beta}, \quad (5.17)$$

then the differential cross section for a given magnification in a flux-limited sample is

$$d\sigma_{\text{fl}}(M) \propto M^{\beta-2} d \ln M, \quad (5.18)$$

where we have used the scaling $\sigma(|M| > M_0) \propto M_0^{-2}$ from equation (5.16). If bright quasars have a steep luminosity function ($\beta \gtrsim 2$; Schmidt and Green 1983), then the observed sample of lensed quasars could be dominated by high-magnification events. In fact, the bright end of the quasar luminosity function could be populated largely by magnified faint sources. Moreover, there would be a tendency for these magnified sources to be associated with foreground galaxies (Canizares 1981; Vietri and Ostriker 1983).

The scaling law (5.16) is derived by making a Taylor expansion of the potential in the image plane. The universality of the scaling law is illustrated by the fact that Turner, Ostriker, and Gott (1984) obtained the same result even though they considered a nongeneric catastrophe. In their example of a circularly symmetric lens, the catastrophe in source space degenerates to a *point*. A source located at this position forms a circular image in the shape of a ring around the lens. Since the caustic in image space is still a line, as in the generic catastrophes we have considered, equation (5.14) continues to hold.

So far we have considered a source confined to a plane at constant redshift. If we now allow the redshift to vary as well, we have three control parameters, and this introduces three more types of caustic, the so-called *swallow-tail*, *elliptic umbilic*, and *hyperbolic umbilic* catastrophes (e.g., Berry and Upstill 1980). Cusp catastrophes now form lines in this three-dimensional space, and fold catastrophes form sheets. Figure 10 shows the arrangement corresponding to a lens with an elliptical mass distribution. Note the occurrence of two interpenetrating caustic sheets. The source has to lie inside one of the sheets to produce three images and inside both to produce five images. Also note the two hyperbolic umbilic catastrophes which transfer two cusps from one sheet to the other as they cross. Therefore, far from the lens, the inner sheet has four cusps and the outer none. Figure 5d shows a section at constant redshift in this "far field" regime, while Figure 4d corresponds to a section closer to the lens, between points *A* and *B* in Figure 10, where the second sheet has not yet formed.

If we follow a congruence (or bundle) of rays back from the observer toward the source, the rays may cross one another. The point at which this happens in a given congruence is termed conjugate to the observer and must lie on a caustic sheet. In general, the rays do not focus to a point (which requires nongeneric high symmetry) but to a line. An image that corresponds to a saddle point in the time surface must have at least one conjugate point, while for a maximum there must be at least two conjugate points along the ray.

We can use the same time-delay surface, computed for a complex lensing potential and a particular source redshift, to derive the image properties when the source is at different redshift, simply by rescaling the potential contribution to the arrival time (eq. [2.6]).

VI. IMAGING BY MULTIPLE LENSES

So far we have restricted our attention to the case when there is a single deflector and well-defined angular diameter distances between observer, source, and deflector. Real exam-

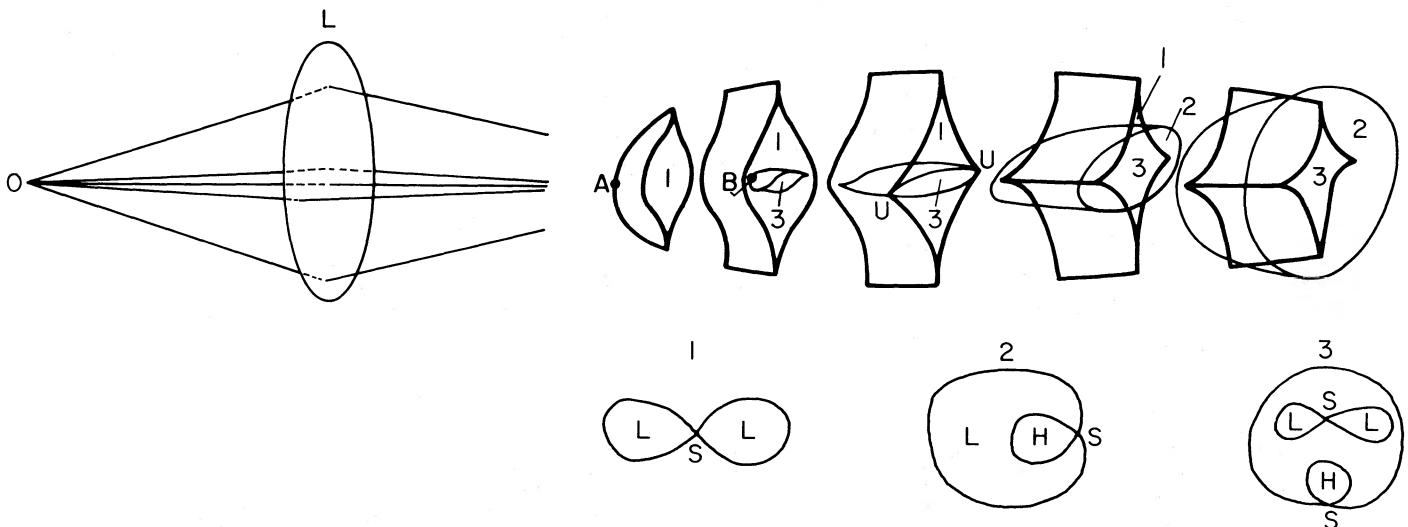


FIG. 10.—Caustic sheets in three-dimensional source space for a fixed observer position *O* and an elliptical lens *L*. The source redshift z_s increases to the right. A bundle of rays reaching *O* in a horizontal plane through the center of the lens have a conjugate point at *A*, which forms the apex of one caustic sheet. A bundle in a vertical plane focuses at *B*, the apex of the second caustic sheet. The lemniscate of Fig. 3 corresponds to a section at constant z_s between *A* and *B*. The source has to be within the sheet to produce three images. As z_s increases, beyond the point *B*, the inner sheet expands and penetrates the outer one at two hyperbolic umbilics marked *U*. Beyond this point, one sheet has four cusps, while the other has none. The limaçon in Fig. 4 corresponds to a source at the right-hand end of the figure, located in region 2. The topologies of the time surface in the regions marked 1, 2, and 3 are shown at the bottom of the figure.

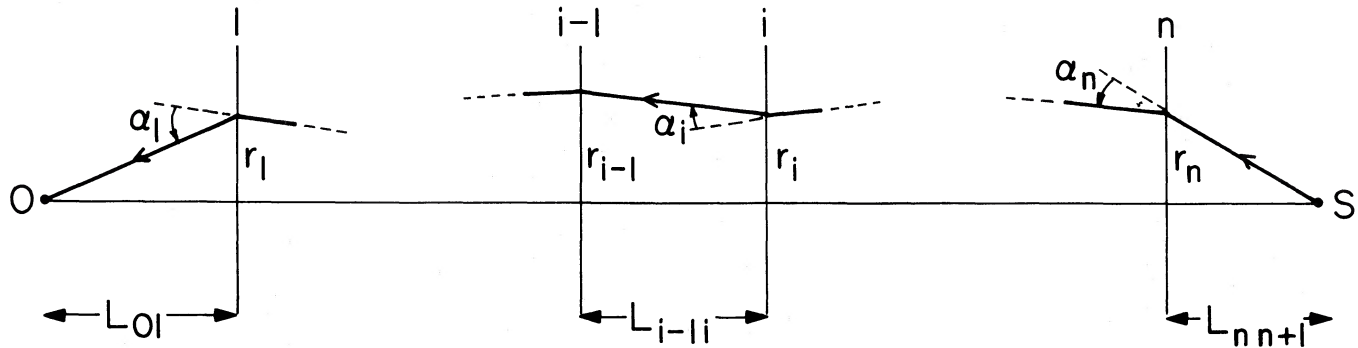


FIG. 11.—Impact parameters r_i and scattering angles α_i at n intervening screens, of a ray from the source S to the observer O . L_{ij} is the angular diameter distance from the i th to the j th lens.

ples of gravitational lensing may be much more complex than this. Consider the case when there are n discrete lenses separating the observer from the source. Let a ray intersect each lens at a proper distance r_i measured from the intersection of the unperturbed ray (Fig. 11). If the angular diameter distance separating the i th lens from the j th lens is d_{ij} and the light travels along null geodesics between lenses, then the time delay along the ray (relative to the unperturbed trajectory) is given by

$$t = \sum_{i=1}^n (1 + z_i) \left[\frac{d_{0i} d_{0i+1}}{2d_{i+1}} \left(\frac{r_{i+1}}{d_{0i+1}} - \frac{r_i}{d_{0i}} \right)^2 - 2 \int \varphi_i ds \right], \quad (6.1)$$

where r_{n+1} is the source position.

Fermat's principle states that we observe images along rays for which the arrival time is an extremum for all possible variations. In this case it is sufficient to vary with respect to the $2n$ coordinates r_i . The images are maxima, minima, or Morse saddles in the corresponding $2n$ -dimensional space. If we perform the variation, then we obtain the n vector equations

$$\left(\frac{r_{i+1}}{d_{0i+1}} - \frac{r_i}{d_{0i}} \right) \frac{d_{0i+1}}{d_{i+1}} - \left(\frac{1 + z_{i-1}}{1 + z_i} \right) \times \left(\frac{r_i}{d_{0i}} - \frac{r_{i-1}}{d_{0i-1}} \right) \frac{d_{0i-1}}{d_{i-1}} + \alpha_i = 0, \quad 1 \leq i \leq n, \quad (6.2)$$

where $\alpha_i(r_i)$ is the deflection associated with the i th screen, and $r_0 = 0$. This reduces to

$$r_i = \frac{d_{0i}}{d_{01}} r_1 + \sum_{j=1}^{i-1} d_{ji} \alpha_j, \quad 2 \leq j \leq n-1, \quad (6.3)$$

which has a straightforward geometrical interpretation.

We follow the spirit of the one-lens calculation and compute the curvature tensor K ,

$$K_{\alpha\beta} = \delta_{\alpha\beta} - \sum_{k=1}^n \frac{d_{0k} d_{kn+1}}{d_{0n+1}} C_{\alpha\beta}^k + \sum_{k=1}^{n-1} \sum_{l=k+1}^n \frac{d_{0k} d_{kl} d_{ln+1}}{d_{0n+1}} \sum_{\gamma} C_{\alpha\gamma}^l C_{\gamma\beta}^k - \sum_{k=1}^{n-2} \sum_{l=k+1}^{n-1} \sum_{m=l+1}^n \frac{d_{0k} d_{kl} d_{lm} d_{mn+1}}{d_{0n+1}} \sum_{\gamma\delta} C_{\alpha\gamma}^m C_{\gamma\delta}^l C_{\delta\beta}^k + \dots, \quad (6.4)$$

where the tensor $C_{\alpha\beta}^k = \partial \alpha_k / \partial r_\beta^k$. The first sum on the right-hand side of equation (6.4) describes the separate focusing of the

individual lenses. The second sum accounts for the change in the final magnification when a deflection caused by one lens changes the deflection caused by a subsequent lens. Succeeding sums describe higher order interactions. The nonlinear terms introduce an important change. Although the individual 2×2 matrices C^l are symmetric, their products are not, and so the curvature tensor K is also *not symmetric in general*. This means that the source position θ_s cannot be the gradient of a scalar function of the image position θ_i as is true in the case of a single lens. Another change introduced when there is more than one lens plane is that in general a small image is related to its source by a *rotation* in addition to an expansion and a shear. This may provide an important diagnostic of multiple lensing (cf. § II).

In the continuum limit, the multilens equations must be replaced by the optical scalar equations of Sachs (1961) (cf. also Alcock and Anderson 1984). These equations are usually presented in the form of propagation equations for the rate of expansion and shear of a congruence of null geodesics passing through a point. In our case, we are interested in rays that reach the observer, and so we must consider the evolution of the congruence backward in time (or, more properly, affine parameter λ). In Newtonian language, we relate r , the small transverse displacement of a ray (measured in local coordinates) from some fiducial ray, to its rate of change of transverse displacement (velocity), $dr/d\lambda$, by the equation

$$\frac{dr}{d\lambda} = \begin{pmatrix} \theta + \sigma_r & \sigma_i \\ \sigma_i & \theta - \sigma_r \end{pmatrix} \cdot r, \quad (6.5)$$

where θ is the rate of expansion and $\sigma = \sigma_r + i\sigma_i$ is a complex representation of the rate of the shear. Note that there is no antisymmetric part of the matrix (angular velocity) in equation (6.5).

The quantities θ and σ evolve according to the propagation equations

$$\frac{d\theta}{d\lambda} + \theta^2 + |\sigma|^2 = -(\varphi_{,11} + \varphi_{,22}) = -4\pi\rho, \quad (6.6)$$

$$\frac{d\sigma}{d\lambda} + 2\theta\sigma = -\varphi_{,11} + \varphi_{,22} - 2i\varphi_{,12},$$

where the second derivatives of the local Newtonian potential are well defined locally.

However, we are mostly interested in the expansion, shear, and rotation of the image as described above. Let us relate the transverse displacement of a neighboring ray to a fiducial ray

at some affine parameter λ (measured backward along the fiducial ray) to the angle this ray makes with the fiducial ray at the observer, $(dr/d\lambda)_0$, by a second matrix equation,

$$r = \begin{pmatrix} \kappa_r + \mu_r & \mu_i + \kappa_i \\ \mu_i - \kappa_i & \kappa_r - \mu_r \end{pmatrix} \cdot \left(\frac{dr}{d\lambda} \right)_0. \quad (6.7)$$

In this equation, the real part of κ , viz., κ_r , describes the expansion of the image; the imaginary part, κ_i , is due to rotation of the image; and the complex quantity μ corresponds to the shear of the image (cf. eq. [2.13], which gives the diagonalized form of the matrix with no rotation). The complex quantities κ and μ satisfy propagation equations

$$\frac{d\kappa}{d\lambda} = \theta\kappa + \bar{\sigma}\mu, \quad \frac{d\mu}{d\lambda} = \theta\mu + \sigma\kappa \quad (6.8)$$

(cf. Penrose 1966). The magnification, equation (2.15), must now be replaced by

$$M = (\kappa\bar{\kappa} - \mu\bar{\mu})^{-1}. \quad (6.9)$$

The advantage of using the optical scalar equations is that they can be used to identify the location of the caustics in an inhomogeneous universe. The congruence emanating from the observer will be focused according to equations (6.6) by the matter it passes through and by the shearing action of the matter outside the beam. A conjugate point is produced if the rate of expansion diverges, i.e., $\theta \rightarrow -\infty$ (cf. Hawking and Ellis 1973). Equivalently, the transformation tensor K_{ij} becomes singular (i.e., $|\kappa| = |\mu|$). Individual rays may pass through several conjugate points, and the loci of these conjugate points are the caustic surfaces discussed in § V. (Note, however, that not all rays produce foci as they cross a caustic surface.)

We can use this approach to understand qualitatively the influence of small matter perturbations along a ray on the shape of a caustic. If the perturbation has a surface density comparable to the critical density introduced in equation (2.5), then it may produce a drastic change in the shape of the caustic and perhaps create additional foci. However, smaller perturbations will merely wrinkle the caustic surfaces and will not alter their overall topology. For this reason, we believe that estimates of high-magnification cross sections computed according to the method outlined in the preceding section assuming a smooth universe will also be appropriate for mild inhomogeneity.

It then becomes of interest to determine the conditions of inhomogeneity under which the topological results of §§ III and IV are strictly preserved. Let us introduce a screen somewhere in between the source and the observer. Suppose the location can be chosen such that each point on the screen can be connected by only one ray to the observer. Similarly, let

each point on the screen be connected by just one ray to the source. Then we can define a time delay $\tau(\theta_i)$ for a virtual ray that propagates along a geodesic from the source to the screen and along a different geodesic from the screen to the observer. The conditions for this construction to be possible are that (a) there should be no caustic surfaces between the observer and the screen and (b) all rays connecting the observer to the source plane should pass through no more than two conjugate points. If these conditions are met, $\tau(\theta_i)$ can be uniquely defined and the topological properties of the time surface are similar to those described for the single-lens case. In particular, maxima, minima, and saddle points can be distinguished, and have the same parities as before. Unfortunately, rotation of the congruence may make it difficult to distinguish maxima from minima observationally.

When the rays connecting the source to the observer pass through several conjugate points, the caustic structure becomes much more complex. However, it remains true that the first image to vary in response to a change in the source will still have positive (i.e., the majority) parity. To show this, let us assume that the parity of the first image to vary is in fact negative, in which case there would be at least one conjugate point along the ray between the observer and the source. The construction in Figure 12 shows that it should then be possible to find a virtual ray with less time delay than the reference geodesic. However, this is not possible, since the first image must correspond to a global minimum in the time surface. Therefore, there can be no conjugate points, and the parity must be positive.

VII. OBSERVATIONAL IMPLICATIONS

The primary motivation for this investigation is the fact that none of the gravitational lens candidates has been understood satisfactorily. The image separations are too large to be explained in terms of galaxy lenses, most known examples of lensing violate the odd-number theorem, and in many cases plausible lenses are not seen in the field of the lensed images. It is therefore imperative to decide whether or not the difficulties are simply associated with having a far less regular distribution of lensing mass along the line of sight than is assumed in the models, or instead are an indication that the models are incorrect in a *qualitative* sense. For example, these observations may herald the existence of more exotic forms of matter or a more complex topological structure of spacetime than usually assumed. To this end, we have concentrated on topological invariants of the image geometry, such as the arrival-time sequence and image parities. We have also made a detailed investigation of certain "universal" characteristics of high-amplification events in the vicinity of caustics.

There is a simple but qualitatively powerful theoretical pre-

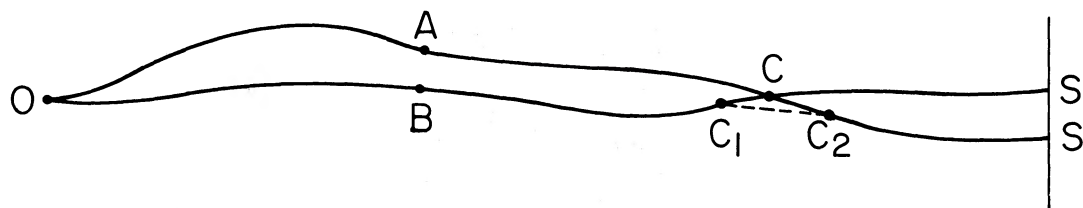


FIG. 12.—Construction to demonstrate that the first image to vary cannot have negative parity. $SCAO$ is a null geodesic from the source S to the observer O , and $S'CBO$ is a neighboring null geodesic that also reaches O after intersecting the first geodesic at the conjugate point C . To second order, the time delays along CAO and CBO are equal, but the time delay along C_1C_2 is less than that along $C_1C + CC_2$. Hence the time along OBC_1C_2S is less than that along $OACSC_2$. Therefore, the geodesic $OACS$ cannot correspond to a global minimum in the time delay.

diction that transparent lenses always produce an *odd* number of images (e.g., Burke 1981). It is most disturbing that we usually observe an *even* number of images. Five resolutions of this discrepancy have been advanced, none of them compelling.

1. The missing images are too faint to have been detected. Here there are two possibilities. The pairs of bright images may straddle a fold caustic and be highly amplified, with the odd image having magnification $M \sim 1$. If so, our discussion of caustics becomes highly relevant and the asymptotic cross section formula, equation (5.16), should be useful. Alternatively, the pairs of images may have $M \sim 1$ and the missing image may be highly deamplified by its proximity to a deep potential well such as a galaxy core (cf. Narayan, Blandford, and Nityananda 1984).

2. The lensing potentials have a much larger size than typical galaxies, and the missing images are far away from the observed images (Narayan, Blandford, and Nityananda 1984). In this scenario, the separation of the observed images is small compared with the scale of the lens, and again our discussion of caustics should be relevant. The apparent homogeneity of the universe on scales $\gtrsim 30$ Mpc argues against the missing images being too distant.

3. Some rays may be strongly absorbed by passing through the center of a galaxy. This is, however, unlikely to be a consideration at radio wavelengths.

4. The potential may be singular, in which case the odd-number theorem does not apply. We have shown in this paper how the two most popular candidates, viz., black holes and strings, can be distinguished with the help of image parities (§ II, Figs. 4 and 5).

5. The unobserved rays may intersect stars within the core of a lensing galaxy (Chang and Refsdal 1984; Subramanian, Chitre, and Narasimha 1985). This explanation fails if the source is sufficiently extended, as in the case of broad emission line regions and radio components of quasars, or if the optical depth to "minilensing" is large (e.g., Nityananda and Ostriker 1984), as will be true for lines of sight through the center of a galaxy. The ideas developed in this paper may be applicable to minilensing, where the brightest subimages will occur near caustics. However, the network of caustics will be highly irregular in this case, and statistical methods are needed.

This last possibility highlights an important restriction. We have implicitly assumed that the lensing potential is smooth, at least on the scale of the separation of the brightest images. If, instead, the projected surface density of the lensing matter is highly granular, then the scaling laws we have given cannot be used. The observation that the A_1 and A_2 images in Q1115+080 have similar apparent magnitudes indicates that the potential is fairly smooth in this object.

We have emphasized in this paper that it is important to monitor the variability of gravitational lens images, since the order of arrival times contains important information about the geometry, particularly in combination with image parities. Various authors have advocated that the quantitative value of the delay will provide an accurate estimate of the Hubble constant H_0 . We agree with those who are skeptical of this (e.g., Alcock and Anderson 1984; Falco, Gorenstein, and Shapiro 1984). It has been our experience that fairly small changes in the lensing potential may introduce much larger differences in the delays than in the image properties. This is most easily seen by considering the arrival-time surface and realizing that

observations can give only partial information about the locations and *relative* curvatures of some of the extrema. Therefore, to deduce H_0 from time delays, one will need to make (possibly unwarranted) assumptions about the nature and distribution of the lensing matter.

Most of our theoretical development as well as much of the earlier work in the field has been predicated on the assumption that the deflecting mass is localized in redshift. We believe that this is likely to be a good approximation in most cases simply because the probability of lensing is known to be small. However, we cannot be sure about this until we determine the slope of the distribution function of lens surface densities. We have shown in § VI that our topological results and scaling laws should be valid even in the presence of mild inhomogeneity along the line of sight, or if there are several "subcritical" lenses in a situation where multiple imaging ceases in the absence of any one of the lenses. Another assumption is that the lensing matter is stationary during the time taken by the light to cross it. This is quite valid for conventional lenses such as stars, galaxies, or clusters, whose motions are subrelativistic, but could be a limitation in the case of cosmic strings. Moving lenses can produce interesting variability in quasars (Chang and Refsdal 1979; Gott 1981; Hogan and Narayan 1984; Subramanian, Chitre, and Narasimha 1985).

We have emphasized the probable importance of caustic surfaces and discussed the details of multiple imaging of sources located near these surfaces. It is possible that some of the known examples of gravitational lensing are located close to caustics, and so we believe that it is a particularly good observational strategy to search for additional examples of multiple imaging *in the same regions of the sky*. In particular, it is worth seeking examples of close galaxy pairs elongated along their lines of separation. The discovery of further multiple images would help map out the underlying caustic surface and also define the relevant source luminosity function. Moreover, if a quasar were multiply imaged close to a caustic and had VLBI core-jet structure, then velocities in the jet would be magnified into "superluminal" motion parallel to the direction of separation of the pair of merging images (cf. Chitre *et al.* 1984).

As we have mentioned, there is already very good evidence that many lenses are dominated by cosmological dark matter. In fact, even in the best-understood case, viz., Q0957+561, it seems that the lensing mass is not traced by the visible light (Greenfield 1981). If lensing is caused by dark matter, then we have no idea about the mass distribution, and therefore properties of lensed images will be most useful in helping to draw *qualitative* conclusions about the underlying potential. The discovery of multiply imaged compact radio sources whose relative parities can be determined by VLBI is particularly important in this regard. Alternatively, if the host galaxies of lensed quasars have irregular morphologies, these could be resolved by Space Telescope, giving valuable information on image parities.

In summary, the purpose of this paper is, first, to present Fermat's principle as a useful way to understand gravitational lensing and, second, to draw attention to the variety of qualitative and semiquantitative inferences that can be drawn *in a model-independent way* from observations of the parities, relative magnifications, and sequence of arrival times of gravitationally lensed images. It is hoped that these ideas will aid the interpretation of existing and future observations of gravitational lens images.

The importance of applying Fermat's principle to the contemporary problem of gravitational lensing was made clear to us by Rajaram Nityananda. We are indebted to him for this and for other insights that he has shared with us. We also thank Peter Quinn for help with computer graphics, Richard

Price for discussions on the optical scalar equations, Craig Hogan and Bill Saslaw for comments on the manuscript, and Charles Lawrence for general discussions on gravitational lenses. Support for this work was provided by the National Science Foundation under grant AST84-15355.

REFERENCES

- Alcock, C., and Anderson, N. 1984, *Ap. J. (Letters)*, **291**, L29.
 Berry, M. V., and Upstill, C. 1980, *Progress in Optics XVIII*, p. 257.
 Blandford, R. D., and Jaroszyński, M. 1981, *Ap. J.*, **246**, 1.
 Bourassa, R. R., and Kantowski, R. 1975, *Ap. J.*, **195**, 13.
 Burke, B. F. 1984, *Comments Ap.*, **10**, 75.
 Burke, W. L. 1981, *Ap. J. (Letters)*, **244**, L1.
 Canizares, C. R. 1981, *Nature*, **291**, 620.
 Chang, K., and Refsdal, S. 1979, *Nature*, **282**, 561.
 ———, 1984, *Astr. Ap.*, **132**, 168.
 Chitre, S. M., Narasimha, D., Narlikar, J. V., and Subramanian, K. 1984, *Astr. Ap.*, **139**, 289.
 Dyer, C. C., and Roeder, R. C. 1973, *Ap. J. (Letters)*, **180**, L31.
 Falco, E. E., Gorenstein, M. V., and Shapiro, I. I. 1984, *Ap. J. (Letters)*, **289**, L1.
 Gorenstein, M. V., et al. 1983, *Science*, **219**, 54.
 Gorenstein, M. V., et al. 1984, *Ap. J.*, **287**, 538.
 Gott, J. R. 1981, *Ap. J.*, **243**, 140.
 ———, 1984, *Ap. J.*, **288**, 422.
 Greenfield, P. E. 1981, unpublished Ph.D. thesis, Massachusetts Institute of Technology.
 Gunn, J. E. 1981, *Ann. NY Acad. Sci.*, **375**, 287.
 Hawking, S. W., and Ellis, G. F. R. 1973, *The Large Scale Structure of Space-Time* (Cambridge: Cambridge University Press).
 Hogan, C. J., and Narayan, R. 1984, *M.N.R.A.S.*, **211**, 575.
 Misner, C. W., Thorne, K. S., and Wheeler, J. A. 1973, *Gravitation* (San Francisco: Freeman).
 Narayan, R., Blandford, R., and Nityananda, R. 1984, *Nature*, **310**, 112.
 Nityananda, R. 1986, in preparation.
 Nityananda, R., and Ostriker, J. P. 1984, *J. Ap. Astr.*, **5**, 235.
 Peacock, J. A. 1983, in *Proc. 24th Liège Internat. Ap. Colloquium*, ed. J. P. Swings (Liège: Institut d'Astrophysique, Université de Liège), p. 86.
 Penrose, R. 1966, in *Perspectives in Geometry and Relativity*, ed. B. Hoffmann (Bloomington: Indiana University Press).
 Poston, T., and Stewart, I. N. 1978, *Catastrophe Theory and Its Applications* (London: Pitman).
 Reasenberg, R. D., et al. 1979, *Ap. J. (Letters)*, **234**, L219.
 Rusk, R. E., and Seaquist, E. R. 1985, *A.J.*, **90**, 30.
 Sachs, R. 1961, *Proc. Roy. Soc. London, A*, **264**, 309.
 Schmidt, M., and Green, R. F. 1983, *Ap. J.*, **269**, 352.
 Schneider, D. P., Gunn, J. E., Turner, E. L., Lawrence, C. R., Hewitt, J. N., Schmidt, M., and Burke, B. F. 1986, preprint.
 Schneider, P. 1984, *Astr. Ap.*, **140**, 119.
 ———, 1985, *Astr. Ap.*, **143**, 413.
 Subramanian, K., Chitre, S. M., and Narasimha, D. 1985, *Ap. J.*, **289**, 37.
 Thom, R. 1975, *Structural Stability and Morphogenesis* (Reading, MA: Benjamin).
 Turner, E. L., Ostriker, J. P., and Gott, J. R. 1984, *Ap. J.*, **284**, 1.
 Vietri, M., and Ostriker, J. P. 1983, *Ap. J.*, **267**, 488.
 Vilenkin, A. 1984, *Ap. J. (Letters)*, **282**, L51.
 Weinberg, S. 1972, *Gravitation and Cosmology* (New York: Wiley).
 Young, P., Gunn, J. E., Kristian, J., Oke, J. B., and Westphal, J. A. 1980, *Ap. J.*, **241**, 507.
 Zel'dovich, Ya. B. 1964, *Soviet Astr.—AJ*, **8**, 13.

ROGER BLANDFORD: Theoretical Astrophysics, 130–33 California Institute of Technology, Pasadena, CA 91125

RAMESH NARAYAN: Steward Observatory, University of Arizona, Tucson, AZ 85721